THE ASTROPHYSICAL JOURNAL, 559:123–130, 2001 September 20

BROADBAND OBSERVATIONS OF THE AFTERGLOW OF GRB 000926: OBSERVING THE EFFECT OF INVERSE COMPTON SCATTERING

F. A. HARRISON,[1] S. A. YOST,[1] R. SARI,[2] E. BERGER,[1] T. J. GALAMA,[1] J. HOLTZMAN,[3] T. AXELROD,[4] J. S. BLOOM,[1] R. CHEVALIER,[5] E. COSTA,[6] A. DIERCKS,[1] S. G. DJORGOVSKI,[1] D. A. FRAIL,[7] F. FRONTERA,[6] K. HURLEY,[8] S. R. KULKARNI,[1] P. MCCARTHY,[9] L. PIRO,[7] G. G. POOLEY,[10] P. A. PRICE,[1] D. REICHART,[1] G. R. RICKER,[11] D. SHEPHERD,[7] B. SCHMIDT,[4] F. WALTER,[1] C. WHEELER[12]

Received 2001 March 20; accepted 2001 May 22

ABSTRACT

GRB 000926 has one of the best-studied afterglows to date, with multiple X-ray observations, as well as extensive multifrequency optical and radio coverage. Broadband afterglow observations, spanning from X-ray to radio frequencies, provide a probe of the density structure of the circumburst medium, as well as of the ejecta energetics, geometry, and physical parameters of the relativistic blast wave resulting from the explosion. We present an analysis of *Chandra X-Ray Observatory* observations of this event, along with *Hubble Space Telescope* and radio monitoring data. We combine these data with ground-based optical and IR observations and fit the synthesized afterglow light curve using models where collimated ejecta expand into a surrounding medium. We find that we can explain the broadband light curve with reasonable physical parameters if the cooling is dominated by inverse Compton scattering. For this model, an excess due to inverse Compton scattering appears above the best-fit synchrotron spectrum in the X-ray band. No previous bursts have exhibited this component, and its observation would imply that the GRB exploded in a moderately dense ($n \sim 30$ cm^{-3}) medium, consistent with a diffuse interstellar cloud environment.

Subject headings: gamma rays: bursts — X-rays: individual (GRB 000926)

1. INTRODUCTION

Broadband observations of gamma-ray burst (GRB) afterglows can in principle be used to constrain fundamental physical parameters of the explosion. In the fireball model, a relativistic blast wave expands into the surrounding medium, its hydrodynamical evolution being strongly influenced by the density structure of the medium, as well as by the energy content and geometry (in particular collimation) of the ejecta. The temporal behavior of the afterglow emission, which arises from the shocked gas, depends on the shock evolution and on the partition of energy between the magnetic field and relativistic electrons, and it can therefore probe these physical parameters, given data of sufficient quality.

In this paper, we report the synthesized results from our multifrequency follow-up campaign on the relatively bright GRB 000926. This campaign was aimed at studying the evolution of the afterglow to constrain the model parameters described above. Price et al. (2001) have reported the results from our multiband (*BVRI*) optical monitoring. We combine these data with four epochs taken with the *Hubble Space Telescope* (*HST*) WFPC2, with *Chandra X-Ray Observatory* (*CXO*) target of opportunity (TOO) observations, and with multifrequency radio monitoring from the Very Large Array (VLA),[13] the Ryle Telescope, and the Owens Valley Radio Observatory. We interpret the resulting broadband light curve in the context of a theoretical afterglow model.

2. OBSERVATIONS AND DATA REDUCTION

The Interplanetary Network discovered GRB 000926 on 2000 September 26.993 UT (Hurley et al. 2000; Hurley 2000). The afterglow of this 25 s long event was identified less than a day later (Gorosabel et al. 2000; Dall et al. 2000). The redshift, measured from optical absorption features, is 2.0369 ± 0.0007 (Fynbo et al. 2000; Castro et al. 2000). The afterglow was well monitored in the optical (Price et al. 2001; Fynbo et al. 2001) and was detected in the IR (DiPaola et al. 2000; Fynbo et al. 2001). Here we describe *HST*, *CXO*, and radio observations.

2.1. *HST Observations*

As part of an *HST* cycle 9 program we observed GRB 000926 at four epochs with the Wide Field Planetary

[1] Division of Physics, Mathematics, and Astronomy, 105-24, California Institute of Technology, Pasadena, CA 91125.
[2] Theoretical Astrophysics, 130-33, California Institute of Technology, Pasadena, CA 91125.
[3] Department of Astronomy, New Mexico State University, Box 30001, Department 4500, Las Cruces, NM 88003-8001.
[4] Research School of Astronomy & Astrophysics, Mount Stromlo Observatory, Cotter Road, Weston, ACT 2611, Australia.
[5] Department of Astronomy, University of Virginia, P.O. Box 3818, Charlottesville, VA 22903
[6] Instituto Astrofisica Spaziale, Consiglio Nazionale delle Ricerche, Via Fosso del Cavaliere 100, 00133 Rome, Italy.
[7] National Radio Astronomy Observatory, P.O. Box O, Socorro, NM 87801.
[8] Space Sciences Laboratory, University of California, Berkeley, Berkeley, CA 94720.
[9] Infrared Processing and Analysis Center, 100-22, California Institute of Technology, Pasadena, CA 91125.
[10] Mullard Radio Astronomy Observatory, Cavendish Laboratory, Madingley Road, Cambridge CB3 0HE, England, UK.
[11] Center for Space Research, MIT, Cambridge, MA 02139.
[12] Department of Astronomy, University of Texas at Austin, Austin, TX 78712.

[13] The NRAO is a facility of the National Science Foundation operated under cooperative agreement by Associated Universities, Inc. NRAO operated the VLA.

Camera 2 (WFPC2), with the optical transient (OT) placed on WFPC CCD 3. In the first three epochs we observed at three passbands, corresponding to the F450W, F606W, and F814W filters, and in the final epoch we used only the F606W and F814W filters. These observations took place between October 7.25 (10.26 days after the GRB) and December 16.9 (81.9 days after).

Table 1 shows a log of the *HST* observations, along with the magnitude derived for each filter for the 2 pixel radius region surrounding the OT. We determined the aperture correction using a 2–5 pixel radius, and we quote the corresponding 5 pixel radius magnitude. We calibrated the zero points and converted the WFPC2 values to Johnson-Cousins magnitudes using the color transformations from Holtzman et al. (1995). We estimate the associated calibration uncertainty to be about 0.10 mag in *B*, *V*, and *R* bands and 0.20 mag in the *I* band. To perform the transformations, we have interpolated the three-filter WFPC2 data to obtain photometric points in *B*, *V*, *R*, and *I*. Measurements in only three of the bands are, therefore, truly independent. We tied the WFPC2 calibration to the ground-based data of Price et al. (2001) using their tertiary star at position R.A. $12^{h}04^{m}11\overset{s}{.}75$, decl. $+51°46'56\overset{''}{.}1$ (J2000). The magnitudes we derive for this star agree with those obtained by Price et al. (2001) to within 0.10 mag in *B*, *V*, and *R* and to within 0.20 mag in *I*. Castro et al. (2001, in preparation) provide further details on the image reduction and magnitude calibration.

From flattening in the late-time ($t \gtrsim 10$ days) optical light curve we infer that the *HST* data are contaminated by a contribution from the host galaxy. We do not actually resolve the host in our *HST* images, and we observe flattening even with our small ($0\overset{''}{.}14$) extraction radius. This implies that the host itself is compact or that the constant emission is from a bright knot or filament associated with the host. Future *HST* observations scheduled for late May of 2001 may resolve this feature, and we will present those results elsewhere. To determine the flux from the OT we subtract this constant contribution.

To derive the magnitude for the constant term, we fit the ground-based optical light curve from Price et al. (2001), combined with our *HST* data, to a decaying function with a constant added:

$$F(t, \nu) = F_0 \nu^{\beta}[(t/t_*)^{-\alpha_1 s} + (t/t_*)^{-\alpha_2 s}]^{-1/s} + F_{\rm host}(\nu) \ . \quad (1)$$

The decaying function, taken from Beuermann et al. (1999), has no physical significance but provides a simple and general parametric description of the data. Here α_1 and α_2 are the early- and late-time asymptotic temporal slopes, respectively, t_* is the time of the temporal slope break, s is a parameter that determines the sharpness of the transition, and β is the spectral slope. From the combined ground-based and *HST* data we derive $\alpha_1 = 1.46 \pm 0.11$, $\alpha_2 = 2.38 \pm 0.07$, $t_* = 1.8 \pm 0.1$ days, and $\beta = -1.49 \pm 0.07$. All errors in this paper are 1 σ. The best-fit values for the constant are $F_{\rm host}(B) = 25.77 \pm 0.14$, $F_{\rm host}(V) = 25.60 \pm 0.1$, $F_{\rm host}(R) = 25.38 \pm 0.1$, and $F_{\rm host}(I) = 25.12 \pm 0.10$. We note that our fit values are similar to those derived by Price et al. (2001), but the late-time, high-resolution *HST* data allow us to determine the flux from the compact region near the OT.

We derive the OT magnitudes by subtracting the constant term $F_{\rm host}$, given above for each band, correcting for the foreground Galactic extinction $E_{B-V} = 0.0235$ mag (Schlegel, Finkbeiner, & Davis 1998). Table 2 contains the resulting dereddened, host-subtracted OT flux values converted to μJy. The measurement errors include a contribution (1 σ) of 0.026 (*B*), 0.016 (*V*), 0.018 (*R*), and 0.020 (*I*) μJy added in quadrature to the statistical and systematic calibration errors to reflect the uncertainty in the constant host term derived from the fit.

TABLE 1

WFPC2 *HST* OBSERVATIONS OF THE GRB 000926 OPTICAL AFTERGLOW

Date (2000, UT)	Filter	Exposure time (s)	Magnitude
Oct 7.25	F450	2 × 1100 (1 orbit)	24.98 ± 0.07
Oct 7.35	F606	4 × 1100 (2 orbits)	24.54 ± 0.03
Oct 7.49	F814	4 × 1100 (2 orbits)	23.89 ± 0.03
Oct 16.08	F450	2 × 1100 (1 orbit)	25.82 ± 0.14
Oct 16.18	F606	4 × 1100 (2 orbits)	24.27 ± 0.03
Oct 16.32	F814	4 × 1100 (2 orbits)	24.87 ± 0.05
Oct 25.05	F450	2 × 1100 (1 orbit)	25.59 ± 0.12
Oct 25.21	F606	4 × 1100 (2 orbits)	25.45 ± 0.03
Oct 25.35	F814	4 × 1100 (2 orbits)	24.96 ± 0.05
Dec 16.02.....	F606	6 × 1000 (3 orbits)	25.58 ± 0.03
Dec 16.90.....	F814	4 × 1100 (2 orbits)	25.24 ± 0.07

2.2. *CXO Observations*

The *BeppoSAX* Medium Energy Concentrating Spectrometer (MECS; sensitive from 1.6 to 10 keV) discovered the X-ray afterglow of GRB 000926 in an observation made September 29.03–29.52 (Piro et al. 2000). Garmire et al. (2000) observed the source for 10 ks as part of a Cycle 1 *CXO* program using the ACIS S3 backside-illuminated chip on September 29.674–29.851 (referred to here as *CXO*-P1). Supporting our *HST* cycle 9 program, *CXO* again observed GRB 000926 for 33 ks as a TOO on October 10.176–10.76 UT (*CXO*-P2), also with the transient placed on the ACIS S3 backside-illuminated chip. The afterglow was clearly detected in both of these observations. The transient was not detected by the *BeppoSAX* Low-Energy Concentrating Spectrometer (co-aligned with the MECS, and sensitive in the 0.1–10 keV band); however, the effective exposure time was only 5 ks. Piro et al. (2001) present a detailed spectral analysis of the X-ray data, including combined fits to all pointings.

TABLE 2

OT MAGNITUDES MEASURED BY *HST*

T (Days after GRB)	Frequency (GHz)	Flux ± σ (μJy)
10.3570	6.871×10^{14} (*B*)	0.233 ± 0.039
19.1870	6.871×10^{14} (*B*)	−0.011 ± 0.037
28.2170	6.871×10^{14} (*B*)	0.057 ± 0.039
10.3570	5.499×10^{14} (*V*)	0.257 ± 0.023
19.1870	5.499×10^{14} (*V*)	0.056 ± 0.019
28.2170	5.499×10^{14} (*V*)	0.008 ± 0.018
80.4670	5.499×10^{14} (*V*)	−0.004 ± 0.018
10.3570	4.673×10^{14} (*R*)	0.398 ± 0.029
19.1870	4.673×10^{14} (*R*)	0.072 ± 0.023
28.2170	4.673×10^{14} (*R*)	0.034 ± 0.022
80.4670	4.673×10^{14} (*R*)	−0.004 ± 0.021
10.3570	3.806×10^{14} (*I*)	0.525 ± 0.058
19.1870	3.806×10^{14} (*I*)	0.075 ± 0.044
28.2170	3.806×10^{14} (*I*)	0.053 ± 0.042
80.4670	3.806×10^{14} (*I*)	−0.012 ± 0.048

TABLE 3

X-RAY AFTERGLOW OF GRB 000926

Pointing	Epoch (J2000, UT)	Band (keV)	Flux $\pm \sigma$ (10^{13} ergs cm^{-2} s^{-1})
BeppoSAX	Sep 29.03–29.53	1.5–8	2.23 ± 0.77
CXO - P1	Sep 29.674–29.851	0.2–1.5	0.614 ± 0.063
CXO - P1	Sep 29.674–29.851	1.5–8	0.939 ± 0.14
CXO - P2	Oct 10.176–10.760	0.2–1.5	0.0263 ± 0.008
CXO - P2	Oct 10.176–10.760	1.5–8	0.0364 ± 0.019

TABLE 4

X-RAY TRANSIENT FLUX

T (Days after GRB)	Frequency (GHz)	Flux $\pm \sigma$ (10^2 μJy)
2.7700.....	1.14×10^{17}	3.98 ± 0.594
13.477.....	1.14×10^{17}	0.156 ± 0.035
2.2780.....	7.5×10^{17}	1.78 ± 0.621
2.7700.....	7.5×10^{17}	0.684 ± 0.070
13.477.....	7.5×10^{17}	0.029 ± 0.016

We analyzed the data from *CXO*-P1 and *CXO*-P2 using software provided by the *Chandra X-Ray Observatory* Center (CXC) to filter the events, extract source counts, and subtract background. For the latter we used an annular region surrounding the source. We fitted the two *CXO* pointings separately using a power-law model plus absorption. The best-fit photon spectral index is $\alpha = 1.9 \pm 0.21$ for the *CXO*-P1 data and $\alpha = 2.23 \pm 0.34$ for *CXO*-P2, with best-fit hydrogen column depth $N_{\rm H} = (4.8 \pm 3) \times 10^{20}$ cm^{-2} (*CXO*-P1) and $N_{\rm H} = (3.0 \pm 2.5) \times 10^{20}$ cm^{-2} (*CXO*-P2). We find no evidence of additional absorption in the X-ray spectrum at the redshift of the host ($z = 2.04$). This is consistent with the host $A(V)$ of 0.1 mag derived from model fits to the optical data (see below), if we adopt typical dust-to-gas ratios. For an LMC-like extinction curve, for example, this $A(V)$ corresponds to a column depth of $N_{\rm H} = 2 \times 10^{20}$ cm^{-2} for a host at $z = 2.04$. Given the host redshift, such a low column is not detectable in the X-ray spectrum, and so no correction for absorption in the GRB host is necessary.

The detection statistics in the X-ray are limited, so for the purposes of our modeling we divided the energy range into soft (0.2–1.5 keV) and hard (1.5–8 keV) bands. We converted counts to flux using exposure maps weighted in energy using a photon power-law spectral index of $\alpha = 2$ and $N_{\rm H} = 2.7 \times 10^{20}$ cm^{-2}, corresponding to the value for our own Galaxy, as determined by W3nH.[14] We adopt this value because it is consistent with that derived from our spectral modeling, and we find no significant evidence of additional absorption in the host. For the *BeppoSAX* observation, we used the best-fit spectral model to determine the hard-band flux (the MECS response does not allow a soft-band flux to be determined).

Table 3 shows the flux values, not corrected for Galactic absorption, for the three observations. To determine the center energy for the band, we took the mean, weighted using a photon index of $\alpha = 2$. We determined flux errors by adding in quadrature the statistical error and the error due to the uncertainty in spectral slope. Because the flux is decaying during each observation interval, we weight the time of the observation by t^{-2} and average to determine the mean epoch. Table 4 lists the center frequencies and flux values for the X-ray transient (converted to microjanskys), where we have corrected for Galactic absorption.

2.3. *Radio Observations*

We obtained radio observations at frequencies from 1.43 to 100 GHz at a number of facilities: the Owens Valley Radio Observatory Interferometer (OVRO), the Ryle Telescope, and the VLA. Table 5 summarizes these observations, organized by frequency. The 98.48 GHz data were taken at OVRO, the 15 GHz data at Ryle, and all other frequencies were observed using the VLA. In performing the observations, reducing the data, and deriving flux errors we adopted the methodology described in detail in Kulkarni et al. (1999), Frail et al. (2000), and Berger et al. (2000). For the OVRO observations, we used the quasar 1726+455 for phase calibration and Uranus for absolute flux calibration.

TABLE 5

RADIO OBSERVATIONS OF GRB 000926

Frequency (GHz)	Epoch (J2000, UT)	Flux $\pm \sigma$ (μJy)
98.48	Sep 29.708	3410 ± 1020
	Oct 1.708	1890 ± 750
22.5	Oct 4.186	1415 ± 185
	Oct 5.216	1320 ± 240
	Oct 16.721	480 ± 230
15.0	Sep 28.81	490 ± 230
	Sep 30.91	-320 ± 520
	Oct 1.69	820 ± 390
	Oct 5.751	460 ± 330
	Oct 11.751	340 ± 220
8.46	Sep 28.17	666 ± 60
	Sep 28.97	150 ± 55
	Sep 29.726	368 ± 26
	Oct 4.186	440 ± 34
	Oct 5.216	566 ± 34
	Oct 7.771	564 ± 76
	Oct 8.291	143 ± 77
	Oct 10.281	242 ± 130
	Oct 12.771	644 ± 126
	Oct 15.681	379 ± 36
	Oct 23.161	277 ± 34
	Oct 27.131	170 ± 79
	Oct 30.181	192 ± 41
	Nov 26.64	143 ± 35
	Dec 18.95	160 ± 21
	Jan 29.44	10 ± 40
	Feb 9.73	71 ± 12
4.86	Sep 28.17	90 ± 67
	Sep 28.97	100 ± 45
	Sep 29.726	280 ± 29
	Oct 4.186	248 ± 30
	Oct 7.741	395 ± 61
	Oct 8.701	370 ± 70
	Oct 30.201	210 ± 33
	Nov 18.03	131 ± 45
	Jan 6.53	62 ± 42
	Feb 2.47	54 ± 41
	Feb 19.28	126 ± 23
1.43	Dec 16.58	96 ± 46

[14] W3nH is available at http://heasarc.gsfc.nasa.gov.

3. AFTERGLOW MODEL

To interpret the broadband light curve we employ a model for the emission from the relativistic shock (resulting from the GRB explosion) as it expands into the surrounding medium. Our modeling is quite comprehensive. It allows for either a constant-density medium, which we refer to as the ISM model, or for a density depending on radius as $\rho = Ar^{-2}$, referred to as the wind model because this profile would be produced by a stellar progenitor's wind (Chevalier & Li 1999). We also allow for either isotropic or collimated ejecta, and we fit for extinction in the host galaxy. We include the effects of inverse Compton (IC) scattering on the evolution of the synchrotron spectrum, as well as the contribution of IC emission to the observed spectrum. IC scattering is not included in most models used to fit GRB afterglows, but if the ambient medium is of sufficiently high density it becomes an important effect. Compton emission can dominate the total afterglow cooling rate for months after the event and can even be directly observed in the X-ray (Panaitescu & Kumar 2000; Sari & Esin 2001).

We calculate the shock emission at a given time and frequency from a number of fundamental parameters: the initial isotropic equivalent energy E in the shock, the electron power-law slope p, the electron and magnetic field energy fractions ϵ_e and ϵ_B, respectively, and the density of the circumburst medium. We employ the equations given by Sari, Piran, & Narayan (1998) and Granot, Piran, & Sari (1999a, 1999b) to determine the evolution of the synchrotron spectrum for the ISM model and the equations given by Chevalier & Li (1999, 2000) for the wind model. We include the effect of inverse Compton scattering using the treatment given by Sari & Esin (2001). We calculate the time at which collimation becomes evident ($\theta = 1/\Gamma$, where Γ is the Lorentz factor of the ejecta) and the subsequent spectral evolution using Sari, Piran, & Halpern (1999). For the host extinction we use the parameterizations of $A(V)$ of Cardelli, Clayton, & Mathis (1989) and Fitzpatrick & Massa (1998), joined using the formula from Reichart (1999) in the rest-frame optical/UV and absorption cross sections given by Morrison & McCammon (1983) in the rest-frame X-ray. We consider both LMC- and SMC-like extinction laws. To fit the broadband light curve we vary the fundamental parameters, iterating to minimize χ^2.

At any given time the synchrotron emission, which dominates at most energies, has a spectrum characterized by a number of breaks: a low-frequency rollover due to self-absorption at frequency ν_a, a peak at frequency ν_m due to the peak energy in the electron distribution, and a cooling break at ν_c, where radiative energy losses become a significant fraction of the electron energy. These breaks evolve in time as the shock evolves, producing frequency-dependent breaks in the light curve. In the case of collimated ejecta, the light curve will begin to steepen when θ is smaller than the angle into which the emission is beamed because of relativistic effects ($1/\Gamma$, where Γ is the Lorentz factor). We use a sharp transition for this "jet break" and employ spherical evolution laws up until the time of the break. After the jet transition we assume that the ejecta expand laterally, and we employ the appropriate asymptotic formulae until the time the ejecta become nonrelativistic. The transition to the nonrelativistic evolution is again treated as sharp.

The inverse Compton component is also characterized by a series of spectral breaks. With the synchrotron spectrum as the photon source, Sari & Esin (2001) find that the upscattered component is characterized by three breaks: at $\nu_a^{\rm IC} \sim 2\min(\gamma_c, \gamma_m)^2\nu_a$, at $\nu_m^{\rm IC} \sim 2\gamma_m^2\nu_m$, and at $\nu_c^{\rm IC} \sim 2\gamma_c^2\nu_c$, where γ_m is the characteristic Lorentz factor of the electrons emitting with peak frequency ν_m. We adopt a spectral shape for the IC component similar to that of the synchrotron spectrum, but with the breaks given by the values in Sari & Esin (2001). This provides a good approximation to the IC component spectral shape except at $\nu < \nu_a^{\rm IC}$, but for our data this is not a concern (see below). Between $\nu_m^{\rm IC}$ and $\nu_c^{\rm IC}$ there is only a logarithmic correction, which we ignore.

4. FITS TO THE BROADBAND GRB 000926 LIGHT CURVE

We fitted the broadband GRB 000926 light curve employing the afterglow model described above. In addition to the data in Tables 1–4, we included the ground-based optical points given in Price et al. (2001), as well as J-band data from DiPaola et al. (2000) and J-, H-, K'- and K-band points from Fynbo et al. (2001). We converted the K' points to K using the prescription in Wainscoat & Cowie (1992). All the data were corrected for absorption in our Galaxy, and in the case of the optical data we subtracted the contribution from the host. The uncertainty in the radio flux is dominated by interstellar scintillation over the timescales of interest here. In calculating the χ^2 for the fit, we added an uncertainty to the radio fluxes based on the scintillation envelopes calculated using the fireball size derived from the model. We excluded the first 8.46 GHz data point from the fits, as it is likely associated with a separate component from the reverse shock (see below).

We considered several possible cases in fitting the data: ISM or wind model for the surrounding medium and two cases for the IC emission. The need to consider two cases arises from the fact that for the same synchrotron emission spectrum, Sari & Esin (2001) find two possible IC solutions. These correspond to the two limits $\eta\epsilon_e/\epsilon_B \equiv f \ll 1$ and $f \gg 1$, where ϵ_e and ϵ_B are the fractions of the total explosion energy that go into accelerating shocked electrons and amplifying the postshock magnetic field, respectively. Here η is the fraction of electron energy radiated away, so it describes whether cooling is dominant. If $f \ll 1$ (low IC), the IC cooling rate is unimportant compared to that of synchrotron, whereas if $f \gg 1$ (high IC) inverse Compton cooling dominates the total emission.

Table 6 summarizes the physical parameters corresponding to the best fit for each model. All models we considered required the ejecta to be collimated in order to explain the break in the optical light curve at 1–2 days. In the optical, this break is roughly independent of frequency. Extinction of $A(V) \sim 0.1$–0.2 mag, presumably due to the host galaxy, is required to fit the optical spectrum in three out of four cases. We employed an LMC-like curve for the models; however, the magnitude of the extinction is relatively insensitive to the extinction law. Price et al. (2001) derived similar values for collimation and extinction based on fits to the optical data alone.

The model that best represents the broadband data is a constant-density ISM with the high-IC solution. Figures 1*a* and 1*b* show the broadband spectrum around days 2 and 10, respectively, with the best-fit model overplotted. The dot-dashed lines show the separate contributions from the synchrotron and IC components. Synchrotron emission dominates at optical frequencies and below; however, on both day 2 and day 10 the model predicts an equal or larger

TABLE 6

FIT PARAMETERS FOR LOW- AND HIGH-IC ISM AND WIND MODELS WITH 1 σ ERRORS

Parameter	High-IC ISM	Low-IC ISM	High-IC Wind	Low-IC Wind
χ^2 for 114 data points[c]	124	187	167	244
$t_{\rm jet}$ (days)	1.55 ± 0.14	1.31 ± 0.13	2.53 ± 0.45	1.38 ± 0.41
$t_{\rm nonrel}$ (days)	70 ± 4	112 ± 7	119 ± 26	308 ± 152
$E_{\rm iso}$[a] (10^{52} ergs)	18 ± 2	8.3 ± 0.9	43 ± 7	39 ± 8
n(ISM)/A_* (wind)[b]	27 ± 3 cm^{-3}	1.6 ± 0.2 cm^{-3}	3.5 ± 0.4	0.26 ± 0.02
p	2.43 ± 0.06	2.20 ± 0.04	3.08 ± 0.03	2.25 ± 0.03
ϵ_e (fraction of E)	0.30 ± 0.05	0.16 ± 0.02	0.16 ± 0.01	0.018 ± 0.003
ϵ_B (fraction of E)	0.008 ± 0.003	1.0	0.005 ± 0.002	1.0
$\theta_{\rm jet}$ (rad)	0.137 ± 0.004	0.099 ± 0.003	0.103 ± 0.002	0.047 ± 0.003
Host $A(V)$	0.12 ± 0.02	0.20 ± 0.02	0.00 ± 0.01	0.20 ± 0.02

[a] Isotropic equivalent blast wave energy (not corrected for collimation). See text for details.
[b] $\rho = A_*(5 \times 10^{11})r^{-2}$ g cm^{-1}.
[c] First 8.46 GHz data point excluded as an outlier.

contribution to the X-ray data from IC scattering. From Figure 1 it is evident that the approximation to the IC contribution made by assuming that it has the same shape as the synchrotron is not an issue in fitting the data. As mentioned above, the error in this approximation is only significant below $\nu_a^{\rm IC}$, and for the parameters we derive the synchrotron dominates the total flux in this region by several orders of magnitude. Figures 2, 3, and 4 show the X-ray, optical, and radio light curves. The χ^2 for the fit is 124 for 114 degrees of freedom.

The first column of data in Table 6 lists the physical parameters for the best-fit high-IC solution. The derived parameters are all reasonable, although we note that an ϵ_e of 0.30 is only marginally consistent with the assumption of adiabatic evolution inherent in our model. While this will not alter our basic conclusions, in future work we will expand the model to include partly radiative blast waves (see Sari 1997 and Cohen, Piran, & Sari 1998 for treatments of the afterglow evolution in this case).

The isotropic equivalent energy in the blast wave ($E_{\rm iso}$ in Table 6) of 1.8×10^{53} ergs is valid for $t \gtrsim 1$ day. We use an adiabatic model to fit the data, which assumes that the total energy is constant in time. While this is approximately valid at $t \gtrsim 1$–2 days (i.e., for the majority of our data), the energy we derive will not represent the total *initial* blast wave energy, because significant energy is lost to radiation at early times. In particular, in the high-IC case the shock wave radiates early on a significant amount of energy, emitted as MeV gamma rays. Using the equations in Cohen et al. (1998), we estimate the energy in the initial fireball to be about 5 times higher than that associated with the adiabatically expanding blast wave at a few days, or $E_{\rm init} \sim 1 \times 10^{54}$ ergs. The observed isotropic energy release in the gamma-ray burst itself was $E_\gamma = 3 \times 10^{53}$ ergs (Hurley et al. 2000, Hurley 2000). Recent theoretical work suggests that the internal shock process producing the GRB should radiate less energy than the blast wave, except under extreme physical conditions (Beloborodov 2000; Koba-

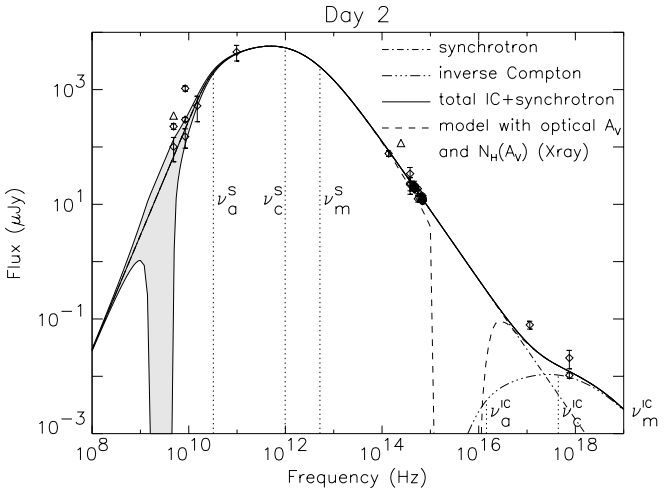

FIG. 1*a*

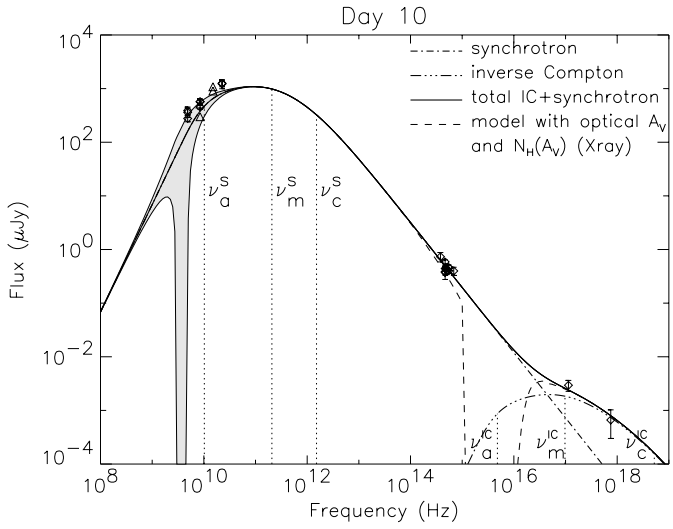

FIG. 1*b*

FIG. 1.—(*a*) Broadband spectrum of the GRB 000926 afterglow on day 2 (after the jet break). All data taken between days 1 and 3 are included, where we have used the model calculations to extrapolate the points forward or backward in time. The relative error seen in the graph therefore represents the true deviation of the observed data from the model at the exact time of the observations. The data, corrected for host extinction, are shown by diamonds, with 1 σ errors, the solid line is the best-fit model without host extinction, and the dashed line shows model plus extinction. The locations of the synchrotron spectral breaks ν_a^s, ν_c^s, and ν_m^s, associated with self-absorption, cooling, and the maximum electron energy, respectively, are indicated. We also indicate the corresponding breaks for the IC spectrum (see Sari & Esin 2001 for details). (*b*) Broadband spectrum of the GRB 000926 afterglow on day 10 (after the jet break).

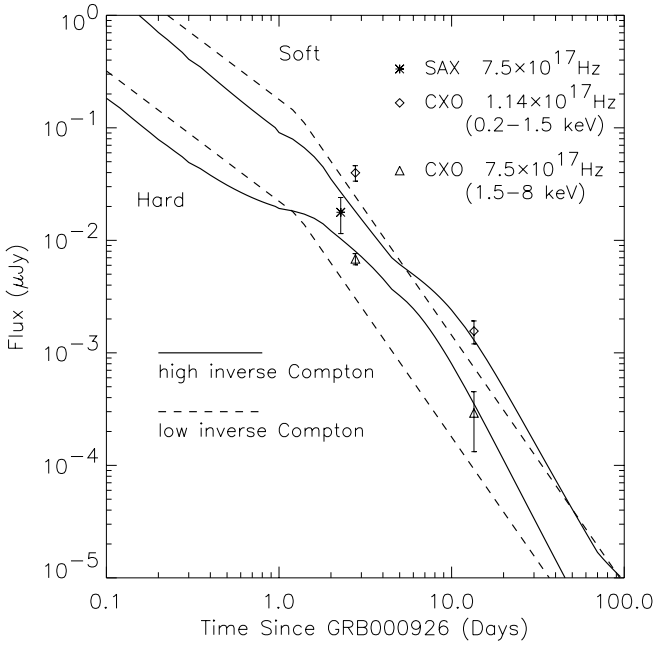

FIG. 2.—X-ray afterglow light curve from *BeppoSAX* and *CXO*. The *CXO* data have been broken into two bands, hard (1.5–8 keV) and soft (0.2–1.5 keV), with center frequencies (weighted with a photon spectral index of $\alpha = 2$) of 7.5×10^{17} Hz and 1.14×10^{17} Hz, respectively. The data have been corrected for absorption in our Galaxy (column of $N_{\rm H} = 2.65 \times 10^{20}$ cm^{-2}). We also show the model calculations for both high- (*solid line*) and low-IC (*dashed line*) constant-density ISM models.

yashi & Sari 2001). The value we derive for the fireball energy is, therefore, reasonable.

To fit the low-IC ISM model, we initially allowed all the physical parameters to vary without limitation. In the low-IC case, the observed emission at all frequencies is from synchrotron radiation alone. The fitting program adjusts the physical parameters in order to reproduce all data with this component. Reproducing the broadband observations requires a large fraction of energy in the postshock magnetic field. The best-fit value of $\epsilon_B = 24$ is unphysical, and so we have fixed ϵ_B at unity—the maximum value physically possible. For either value of ϵ_B the low-IC model provides a poor fit to the data. The χ^2 is 187 for 114 data points when $\epsilon_B = 1$ and 178 for 114 data points when $\epsilon_B = 24$. The largest contribution to the χ^2 comes from the optical data, where the synchrotron component does not fit the data as well as that derived in the high-IC case.

Table 6 provides the physical parameters associated with the best-fit low-IC ISM model for ϵ_B fixed at unity. In addition to the large ϵ_B, the isotropic equivalent energy in the blast wave of 10^{53} ergs in the low-IC case is smaller than the observed gamma-ray energy release. Radiative corrections for this model are much smaller than in the high-IC case, so that the adiabatic value more closely represents the energy in the initial fireball. As pointed out above, $E_\gamma \gtrsim E_{\rm init}$ is hard to accommodate except under extreme conditions.

Figure 2 shows the X-ray data with both high- and low-IC ISM models overplotted. The high-IC case provides a somewhat better fit to the data, because the low-IC case systematically underpredicts the measurements. The X-ray observations alone, however, are not sufficient to indicate the presence of an inverse Compton component in this case. This requires the results from the broadband fit. Our calculations show that the IC scattering hardens the X-ray spec-

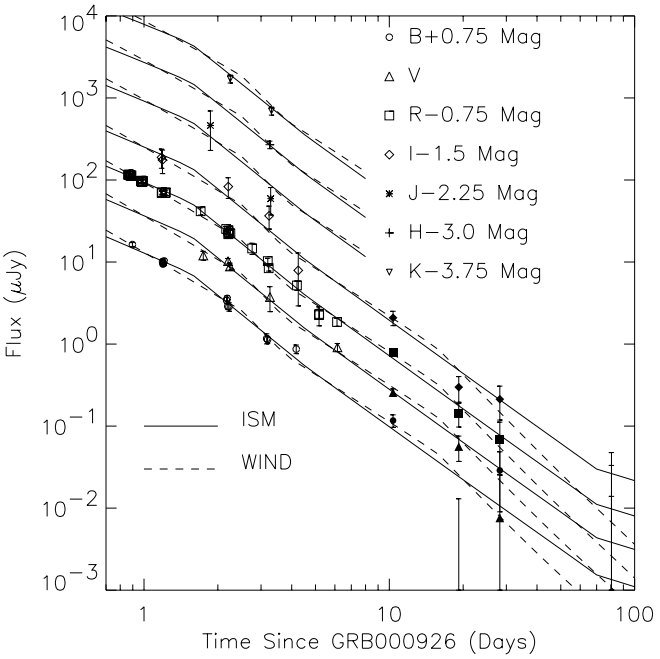

FIG. 3.—Optical/IR afterglow light curve in seven bands. We have subtracted the host contribution, as determined from the late-time *HST* data, and corrected for Galactic extinction. The ISM (*solid lines*) and best-fit wind (*dashed line*) models include the effect of extinction in the host galaxy, as determined by the best-fit value using an extinction curve (dust-to-gas ratio) like that of the LMC.

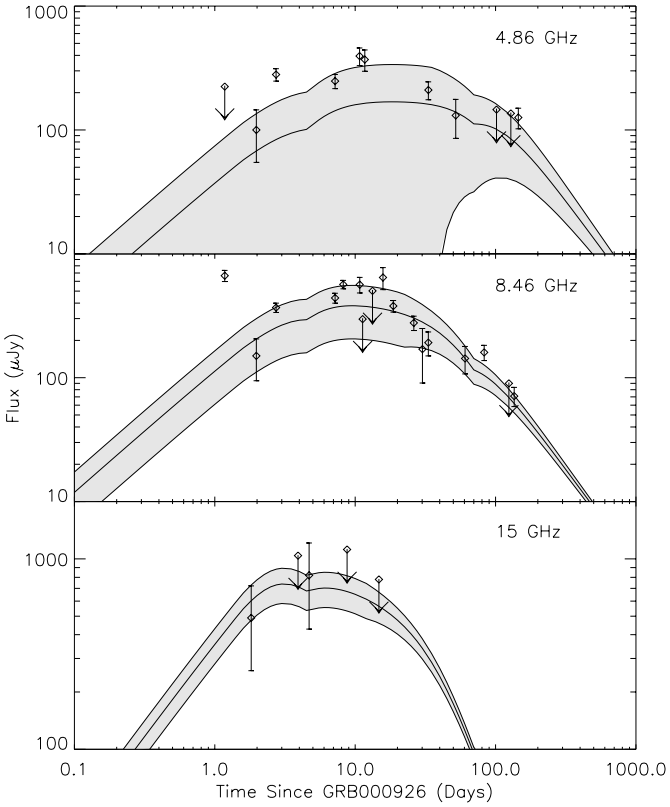

FIG. 4.—Radio light curve at three frequencies. Solid lines show the model calculations based on the high-IC ISM solution. The shaded regions indicate the estimated scintillation envelopes based on the calculated size of the fireball. The upper limits are plotted as 3 σ.

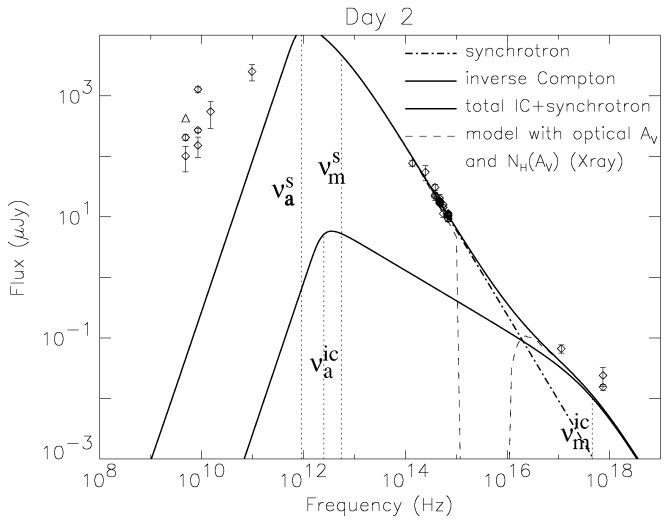

FIG. 5.—Fit to the high-density ($n = 4 \times 10^4$ cm^{-3}) medium of Piro et al. (2001). The solid line shows the model calculations, and the dashed lines show the synchrotron and inverse Compton contributions separately.

trum over some time intervals, compared with the prediction by the low-IC model. There is only marginal evidence for this conclusion in these data; the observed X-ray spectral photon index is 1.9 ± 0.21 compared with the $p/2+1 = 2.2$ associated with the synchrotron component. This emphasizes the role of future, higher significance X-ray observations in confirming the role of IC scattering in GRB afterglows.

We also investigated a wind-density profile in both high- and low-IC regimes. Neither of these cases reproduces the data as well as the high-IC ISM model. The low-IC wind solution has a poor χ^2 of 244 for 114 degrees of freedom. Again we have fixed $\epsilon_B = 1.0$, because the best-fit value of 174 is unphysical. The high-IC wind case also has a large χ^2 of 167 for 114 dof and underpredicts the 5 GHz radio data by a factor of 2–3. It does, however, reproduce the X-ray data reasonably well. We note that early-time optical or high-frequency radio data are particularly important in ruling out the wind model. This is because the light-curve evolution after the jet break is similar for the ISM and wind models. Directly observing the cooling-break evolution provides the greatest leverage, because this evolution is significantly different for wind and ISM models. Generally, this requires optical observations or high-frequency radio observations at early epochs (minutes to hours after the event). Unfortunately, optical coverage of this event began rather late ($t \sim 0.8$ days), but future early-time observations of other events will provide a more sensitive probe of density structure in the surrounding medium.

Finally, we point out that, even for our best-fit (high-IC ISM) solution, the first 8 GHz data point exceeds the model's expectation by a factor of 3.3 (7.9 σ). This discrepancy is worse for the alternative models. Scintillation gains this large are extremely improbable, and it is therefore likely that we are seeing evidence of an additional component due to the reverse shock emission, as was detected in early radio observations of GRB 990123 (Kulkarni et al. 1999).

5. TESTING THE HIGH-DENSITY MODEL FOR GRB 000926

Piro et al. (2001) analyzed the X-ray and optical light curves of GRB 000926 and noted that the spectral and temporal properties cannot be explained using a standard jet model with moderate ISM density. By invoking inverse Compton cooling, we were able to fit the data with a moderate-density medium and relatively standard fireball parameters. In order to describe the X-ray and optical light curves, Piro et al. (2001) invoke moderate collimation of the fireball (opening angle $\theta = 25°$) and a dense ($n = 4 \times 10^4$ cm^{-3}) medium. This high density results in rapid deceleration of the fireball and an early transition to the nonrelativistic regime. These features seemingly reproduce the general characteristics of the high-frequency observations. The high density found by Piro et al. would suggest that the event took place in a molecular cloud, and, further, the low extinction measured in the optical would indicate that the GRB destroyed much of the dust in its vicinity.

The radio data provide an important means of distinguishing these two interpretations. If the fireball expands in a very dense medium, the ejecta decelerate much more rapidly, and at a given time the fireball radius is significantly smaller than for the moderate densities derived in this paper. The self-absorption frequency, easily observed as a cutoff in the radio spectrum, is correspondingly much higher at a given time in the high-density case.

We have fitted a model with the ISM density fixed at $n = 4 \times 10^4$ cm^{-3} and the jet opening angle of $\theta = 25°$ to the broadband data set. We investigated both high-IC and low-IC constant-density solutions and obtained the best fit using the high-IC model. Figure 5 shows the broadband spectrum on day 2, with a comparison of our best fit with the data. The radio data quite clearly exclude the high-density possibility, because the self-absorption frequency is more than a decade higher than we measure. On day 2, the high-density model predicts an 8 GHz radio flux of ~ 0.2 μJy, whereas we measure a flux of 200 μJy. This points out the importance of broadband coverage, including radio, in constraining models for the GRB environment.

6. CONCLUSIONS

GRB 000926 has one of the highest-quality broadband afterglow light curves studied to date. We can explain all the general features using a model of a relativistic shock produced by ejecta collimated to a $\sim 8°$ opening angle. If we correct the isotropic equivalent gamma-ray energy release for this jet angle, we obtain $E_\gamma = E_{\gamma,\,\rm iso}\theta^2/2 = 3 \times 10^{51}$ ergs. This is reasonably accounted for in most currently popular progenitor models. Our observations require extinction in the host galaxy, with a corresponding hydrogen column of $\sim 2 \times 10^{20}$ cm^{-2} if the dust-to-gas ratio is typical of the LMC or SMC. This is consistent with the event taking place in a galactic disk.

We find that an explosion occurring in a spatially homogeneous medium best describes the broadband light curves, provided that the ratio $\eta\epsilon_e/\epsilon_B \gg 1$. This condition implies that Compton emission dominates the total cooling rate and that IC scattering is potentially directly observable in the afterglow spectrum. We do, in fact, find that for our best-fit model IC emission dominates over the synchrotron contribution at 1 keV on the 2–10 day timescales spanned by our X-ray data. Detecting the IC emission in the X-ray band directly implies a lower limit on the density (Panaitescu & Kumar 2000; Sari & Esin 2001), in this case $n \gtrsim 10$ cm^{-3}, and our best fit yields $n = 30$ cm^{-3}. This value for n is higher than the average ISM density in a typical galaxy and is consistent with a diffuse interstellar

cloud, such as those commonly found in star-forming regions. Combining the density with the host N_H derived from our optical observations (again assuming typical dust-to-gas ratios) implies a scale size of 2 pc for the cloud.

We wish to thank Harvey Tananbaum and the *CXO* operations staff for facilitating the *Chandra* TOO observations. We thank Steve Beckwith and the *HST* operations staff for facilitating the WFPC2 observations. F. A. H. acknowledges support from a Presidential Early Career award. S. R. K. and S. G. D. thank NSF for support of their ground-based GRB programs. R. S. is grateful for support from a NASA ATP grant. R. S. and T. J. G. acknowledge support from the Sherman Fairchild Foundation.

REFERENCES

Beloborodov, A. M. 2000, ApJ, 539, L25
Berger, E., et al. 2000, ApJ, 545, 56
Beuermann, K., et al. 1999, A&A, 352, L26
Cardelli, J. A., Clayton, G. C., & Mathis, J. S. 1989, ApJ, 345, 245
Castro, S. M., Djorgovski, S. G., Kulkarni, S. R., Bloom, J. S., Galama, T. J., Harrison, F. A., & Frail, D. A. 2000, GCN Circ. 851 (http://gcn.gsfc.nasa.gov/gcn/gcn3/851.gcn3)
Chevalier, R. A., & Li, Z.-Y. 2000, ApJ, 536, 195
———. 1999, ApJ, 520, L29
Cohen, E., Piran, T., & Sari, R. 1998, ApJ, 509, 717
Dall, T., Fynbo, J. P. U., Pedersen, H., Jensen, B. L., Hjorth, J., & Gorosabel, J. 2000, GCN Circ. 804 (http://gcn.gsfc.nasa.gov/gcn/gcn3/804.gcn3)
DiPaola, A., Speziali, R., Antonelli, L. A., Pedichini, F., D'Alessio, F., Israel, G. L., Lorenzetti, D., & Stella, L. 2000, GCN Circ. 816 (http://gcn.gsfc.nasa.gov/gcn/gcn3/816.gcn3)
Fitzpatrick, E. L., & Massa, D. 1998, AAS, 193, 44.03
Frail, D. A., et al. 2000, ApJ, 538, L129
Fynbo, J. P. U., Møller, P., Gorosabel, J., Hjorth, J., Jensen, B. L., & Pedersen, H. 2000, GCN Circ. 825 (http://gcn.gsfc.nasa.gov/gcn/gcn3/825.gcn3)
Fynbo, J. P. U., et al. 2001, A&A, 373, 796
Garmire, G., Garmire, A., Piro, L., & Garcia, M. R. 2000, GCN Circ. 836 (http://gcn.gsfc.nasa.gov/gcn/gcn3/836.gcn3)
Gorosabel, J., Castro Cerón, J. M., Castro-Tirado, A. J., Greiner, J., Wolf, C., & Lund, N. 2000, GCN Circ. 803 (http://gcn.gsfc.nasa.gov/gcn/gcn3/803.gcn3)
Granot, J., Piran, T., & Sari, R. 1999a, ApJ, 513, 679
———. 1999b, ApJ, 527, 236
Holtzman, J. A., Burrows, C. J., Casertano, S., Hester, J. J., Trauger, J. T., Watson, A. M., & Worthey, G. 1995, PASP, 107, 1065
Hurley, K. 2000, GCN Circ. 802 (http://gcn.gsfc.nasa.gov/gcn/gcn3/802.gcn3)
Hurley, K., Mazets, E., Golenetskii, S., & Cline, T. 2000, GCN Circ. 801 (http://gcn.gsfc.nasa.gov/gcn/gcn3/801.gcn3)
Kobayashi, S., & Sari, R. 2001, ApJ, 551, 934
Kulkarni, S. R., et al. 1999, ApJ, 522, L97
Morrison, R., & McCammon, D. 1983, ApJ, 270, 119
Panaitescu, A., & Kumar, P. 2000, ApJ, 543, 66
Piro, L., et al. 2000, GCN Circ. 812 (http://gcn.gsfc.nasa.gov/gcn/gcn3/812.gcn3)
———. 2001, ApJ, 558, 442
Price, P. A., et al. 2001, ApJ, 549, L7
Reichart, D. 1999, ApJ, 521, L111
Sari, R. 1997, ApJ, 489, L37
Sari, R., & Esin, A. A. 2001, ApJ, 548, 787
Sari, R., Piran, T., & Halpern, J. P. 1999, ApJ, 519, L17
Sari, R., Piran, T., & Narayan, R. 1998, ApJ, 497, L17
Schlegel, D. J., Finkbeiner, D. P., & Davis, M. 1998, ApJ, 500, 525
Wainscoat, R. J., & Cowie, L. L. 1992, AJ, 103, 332